White Rose Research Online

eprints@whiterose.ac.uk
https://eprints.whiterose.ac.uk
Universities of Leeds, Sheffield and York

Deposited via The University of York.

White Rose Research Online URL for this paper:
https://eprints.whiterose.ac.uk/id/eprint/188625/

Version: Published Version

Article:
Frost-Schenk, J., Adsley, P., Laird, A. M. et al. (2022) The impact of ^{17}O$+α$ reaction rate uncertainties on the s-process in rotating massive stars. MONTHLY NOTICES OF THE ROYAL ASTRONOMICAL SOCIETY. 2650–2657. ISSN: 0035-8711

https://doi.org/10.1093/mnras/stac1373

Reuse
This article is distributed under the terms of the Creative Commons Attribution (CC BY) licence. This licence allows you to distribute, remix, tweak, and build upon the work, even commercially, as long as you credit the authors for the original work. More information and the full terms of the licence here:
https://creativecommons.org/licenses/

Takedown
If you consider content in White Rose Research Online to be in breach of UK law, please notify us by emailing eprints@whiterose.ac.uk including the URL of the record and the reason for the withdrawal request.

UNIVERSITY OF LEEDS
University of Sheffield
UNIVERSITY of York

Monthly Notices of the ROYAL ASTRONOMICAL SOCIETY

MNRAS **514,** 2650–2657 (2022) https://doi.org/10.1093/mnras/stac1373
Advance Access publication 2022 May 19

The impact of $^{17}O + \alpha$ reaction rate uncertainties on the s-process in rotating massive stars

J. Frost-Schenk,[1] P. Adsley ,[2,3,4,5] A. M. Laird,[1★] R. Longland,[6,7] C. Angus,[1,8] C. Barton,[1] A. Choplin,[9] C. Aa. Diget,[1] R. Hirschi,[10,11] C. Marshall,[6,7] F. Portillo Chaves [6,7] and K. Setoodehnia[6,7]

[1]*Department of Physics, University of York, York YO10 5DD, UK*
[2]*School of Physics, University of the Witwatersrand, Johannesburg 2050, South Africa*
[3]*iThemba LABS, National Research Foundation, PO Box 722, Somerset West 7129, South Africa*
[4]*Cyclotron Institute, Texas A&M University, College Station, Texas, TX 77843, USA*
[5]*Department of Physics and Astronomy, Texas A&M University, College Station, Texas, TX 77843, USA*
[6]*Department of Physics North Carolina State University, Raleigh, North Carolina, NC 27695-8202, USA*
[7]*Triangle Universities Nuclear Laboratory, Durham, North Carolina, NC 27708-0308, USA*
[8]*TRIUMF, 4004 Wesbrook Mall, Vancouver, BC V6T 2A3, Canada*
[9]*Institut d'Astronomie et d'Astrophysique, Université Libre de Bruxelles, CP 226, B-1050 Brussels, Belgium*
[10]*Astrophysics Group, Lennard-Jones Laboratories, Keele University, Keele ST5 5BG, UK*
[11]*Kavli IPMU (WPI), The University of Tokyo, Kashiwa, Chiba 277-8583, Japan*

Accepted 2022 May 3. Received 2022 May 3; in original form 2022 January 26

ABSTRACT

Massive stars are crucial to galactic chemical evolution for elements heavier than iron. Their contribution at early times in the evolution of the Universe, however, is unclear due to poorly constrained nuclear reaction rates. The competing $^{17}O(\alpha, \gamma)^{21}Ne$ and $^{17}O(\alpha, n)^{20}Ne$ reactions strongly impact weak s-process yields from rotating massive stars at low metallicities. Abundant ^{16}O absorbs neutrons, removing flux from the s-process, and producing ^{17}O. The $^{17}O(\alpha, n)^{20}Ne$ reaction releases neutrons, allowing continued s-process nucleosynthesis, if the $^{17}O(\alpha, \gamma)^{21}Ne$ reaction is sufficiently weak. While published rates are available, they are based on limited indirect experimental data for the relevant temperatures and, more importantly, no uncertainties are provided. The available nuclear physics has been evaluated, and combined with data from a new study of astrophysically relevant ^{21}Ne states using the $^{20}Ne(d, p)^{21}Ne$ reaction. Constraints are placed on the ratio of the $(\alpha, n)/(\alpha, \gamma)$ reaction rates with uncertainties on the rates provided for the first time. The new rates favour the (α, n) reaction and suggest that the weak s-process in rotating low-metallicity stars is likely to continue up to barium and, within the computed uncertainties, even to lead.

Key words: nuclear reactions, nucleosynthesis – stars: rotation.

1 INTRODUCTION

Massive stars are key contributors to the abundance of chemical elements, producing elements up to the iron group via charged-particle reactions during their evolution and subsequent explosion in core-collapse supernovae, and synthesizing elements heavier than iron via neutron-capture reactions. The weak s-process during core-helium (Langer, Arcoragi & Arnould 1989; Prantzos, Hashimoto & Nomoto 1990; Baraffe, El Eid & Prantzos 1992) and to a smaller extent during shell-carbon burning (Raiteri et al. 1991; The, El Eid & Meyer 2007) and possibly the weak r-process in the supernova explosion (Thielemann et al. 2011) produce elements up to the strontium peak in standard, non-rotating, models.

Rotation in massive star models significantly boosts the efficiency of the weak s-process, especially at low metallicity (Pignatari et al. 2008), enhancing production of elements above strontium. With rotation, the helium core contribution to the s-process was shown to increase at the expense of the carbon-burning shell. In the models of Frischknecht et al. (2016), the carbon-burning shell contribution is less than 10 per cent at sub-solar metallicities. During the core helium burning phase, rotation-induced mixing transports ^{12}C and ^{16}O from the He-core to the H-shell, leading to substantial overproduction of ^{13}C and ^{14}N through the CNO cycle. These isotopes are later engulfed by the growing convective He-burning core, leading to a more efficient activation of neutron sources through the $^{14}N(\alpha, \gamma)^{18}F(\beta +)^{18}O(\alpha, \gamma)^{22}Ne(\alpha, n)^{25}Mg$ chain, and the $^{13}C(\alpha, n)$ reaction (Pignatari et al. 2008; Frischknecht et al. 2016; Choplin et al. 2018; Limongi & Chieffi 2018; Banerjee, Heger & Qian 2019). Specifically, Cescutti et al. (2013) have shown that the Sr/Ba scatter at low metallicity of the observed Milky Way halo stars can be reproduced if the contribution of fast rotating massive stars is included.

The contributions of rotating massive stars to chemical evolution are subject to stellar and nuclear uncertainties. One key nuclear uncertainty is the ratio between the $^{17}O(\alpha, n)^{20}Ne$ and $^{17}O(\alpha, \gamma)^{21}Ne$

★ E-mail: alison.laird@york.ac.uk

© The Author(s) 2022.
Published by Oxford University Press on behalf of Royal Astronomical Society. This is an Open Access article distributed under the terms of the Creative Commons Attribution License (http://creativecommons.org/licenses/by/4.0/), which permits unrestricted reuse, distribution, and reproduction in any medium, provided the original work is properly cited.

Downloaded from https://academic.oup.com/mnras/article/514/2/2650/6589423 by guest on 01 July 2022

reaction rates (Frischknecht, Hirschi & Thielemann 2012; Choplin et al. 2018). At all metallicities, ^{16}O is abundant in both the helium-burning core and the shell carbon burning. It is a strong neutron absorber, producing copious amounts of ^{17}O and loss of neutron flux. The neutrons absorbed by ^{16}O may be recovered via the ^{17}O(α, n)^{20}Ne reaction. Alternatively, the ^{17}O(α, γ)^{21}Ne reaction permanently absorbs the neutron, preventing it from contributing to s-process nucleosynthesis. The ^{17}O(α, n)^{20}Ne to ^{17}O(α, γ)^{21}Ne ratio therefore determines the fraction of neutrons released and the strength of the s-process.

At He-core burning temperatures (0.2–0.3 GK), the ^{17}O + α reactions are dominated by resonant contributions from states between E_x = 7600 and 8100 keV ($E_r \approx$ 250–750 keV) in ^{21}Ne. However key properties of the most important states have not been measured. These unknown properties lead to large uncertainties in the reaction rates though no previous rate estimates have provided uncertainties (Caughlan & Fowler 1988; Best et al. 2013). Here, a new calculation of the ^{17}O+α reaction rates is presented, providing realistic uncertainties for the first time. The rates are derived from a rigorous evaluation of excited states in ^{21}Ne based on a new measurement of the ^{20}Ne(d, p)^{21}Ne reaction, together with an evaluation of existing literature.

2 EXISTING LITERATURE ON ^{21}NE LEVELS

Some experimental data on levels in ^{21}Ne are available from studies using a variety of populating reactions. As these works are used in the present paper to constrain the properties of observed levels, they are briefly summarized.

Direct measurements of ^{17}O(α, γ)^{21}Ne (Best et al. 2011; Taggart et al. 2019; Williams et al. 2022) and ^{17}O(α, n)^{20}Ne (Best et al. 2013) have been performed but were not able to observe all states within the Gamow window due to the prohibitively low cross-sections. The ^{17}O(α, γ)^{21}Ne and ^{17}O(α, n)^{20}Ne measurements in forward kinematics of Best et al. (2011, 2013) used anodized tantalum-oxide targets with enriched ^{17}O and a germanium detector. Measurements of the ^{17}O(α, γ)^{21}Ne radiative-capture reaction were performed in inverse kinematics with the DRAGON recoil separator by Taggart et al. (2019) and Williams et al. (2022).

The ^{17}O(α, γ)^{21}Ne measurement of Best et al. (2011) observed three resonances at E_r = 811, 1122, and 1311 keV. The subsequent study of the same reaction by Taggart et al. (2019) observed resonances at E_r = 633, 721, 810, and 1122 keV. Some of the resonance strengths were revised by Williams et al. (2022) based on new DRAGON measurements with higher beam intensities, including an upper limit for the strength of the E_r = 612-keV resonance in ^{17}O(α, γ)^{21}Ne.

Best et al. (2013) also measured the ^{17}O(α, $n_{\rm tot}$)^{20}Ne reaction using tantalum-oxide targets. The neutrons were detected in 20 ^{3}He counters within a polyethylene moderator. The ^{17}O(α, $n_1\gamma$)^{20}Ne reaction was measured by observation of γ rays depopulating the first-excited state of ^{20}Ne. The excitation function was measured between E_{cm} = 650 and 1860 keV. A number of resonance structures were observed and an R-matrix analysis was performed. Rates of the ^{17}O(α, γ)^{21}Ne and ^{17}O(α, n)^{20}Ne reactions were reported. These rates included estimated contributions from unmeasured resonances below the region scanned in the excitation function, making assumptions about unknown spins and parities in combination with known information about levels in ^{21}Ne (Firestone 2015).

A subsequent uncertainty analysis of the measured ^{17}O(α,n)^{20}Ne excitation functions presented in the literature was performed by Mohr (2017), which raised some doubts about the consistency of the data presented in Best et al. (2013) in comparison to historical literature. However, the study found the largest discrepancy was in the high-energy cross-section affecting the reaction rate at temperatures above 1 GK. At those energies, Mohr (2017) suggested that the cross-section presented in Best et al. (2013) should be lowered by a factor of 2–3. At lower energies, though, their data appears to be in better agreement with the literature (see fig. 5 of Mohr (2017)). Furthermore, at the temperatures of interest in the present work (0.2–0.3 GK), the reaction rate is dominated by unobserved resonances that we treat in a rigorous manner and were not considered in Mohr (2017), which focused on applying the statistical model to compute reaction rates.

Additional key information about the excited states has been extracted from earlier measurements, including scattering and transfer studies. Cohn & Fowler (1959) performed a neutron resonance-scattering experiment. Neutrons were produced by bombarding a zirconium tritide and ^{7}Li targets with protons. The incident neutron energies were varied by changing the bombarding energy of the proton beam. Information on excitation energies, widths, and spins and parities for ^{21}Ne levels above the neutron threshold was determined. The uncertainty in the neutron energy scale was less than 5 keV and the neutron energy resolution was around 13 keV. Resonances with widths as small as Γ = 6(2) keV were observed in this experiment.

Various γ-ray studies using reactions such as ^{18}O(α, $n\gamma$)^{21}Ne (Rolfs et al. 1972; Hoffman et al. 1989), ^{12}C(^{13}C,α)^{21}Ne (Hallock et al. 1975; Andritsopoulos et al. 1981), and ^{16}O(^{7}*Li*, *np*)^{21}Ne (Thummerer et al. 2003; Wheldon et al. 2005) provided additional information. Spins and parities of excited levels were assigned on the basis of observed decay branching and angular distributions. The observation of γ-ray decays from neutron-unbound levels in ^{21}Ne can be used in combination with other observables to rule out certain spins and parities since the neutron partial width of a state cannot exceed the γ-ray partial width by a significant factor if a γ-ray transition is observed depopulating the state.

The ^{20}Ne(d, p)^{21}Ne single-neutron transfer reaction has previously been studied by Stanford & Quin (1980). In this experiment, the differential cross-sections and analysing powers of eight states in ^{21}Ne were measured using a vector polarized deuteron beam on an enriched ^{20}Ne gas cell target. The resolution was around 100 keV, largely due to the significant energy loss through the target for the deuteron beam. Large deviations between the calculated differential cross-sections from the DWBA and the experimental data were observed at higher angles. This is likely due to the strong deformation of the ^{20}Ne core. Inelastic excitation of deformed nuclei means that treatment with the DWBA may no longer accurately reflect the observed differential cross-section (e.g. the ^{20}Ne(d, ^{3}He)^{19}F study of Dudek & Edens (1971). For this reason, analysis of the strength of the ^{20}Ne(d, p)^{21}Ne single-neutron transfer reaction should be limited to centre-of-mass angles below around 30°.

3 EXPERIMENTAL DETAILS

The experiment was performed at the Triangle Universities Nuclear Laboratory (TUNL). Deuterons were accelerated to 14 MeV through the tandem accelerator with an energy precision of better than 1 keV. Typical currents recorded with an electron-suppressed beamstop downstream from the target were 300–575 nA, except at the most forward angle where currents were limited to around 90 nA.

The target consisted of ^{20}Ne implanted into a 44 μg cm^{-2} carbon foil with a Ne/C abundance ratio of 4.3 ± 0.3 per cent determined by Rutherford Backscattering Spectrometry. The neon content was monitored with deuteron elastic scattering at $\theta_{\rm lab}$ = 25° after

Downloaded from https://academic.oup.com/mnras/article/514/2/2650/6589423 by guest on 01 July 2022

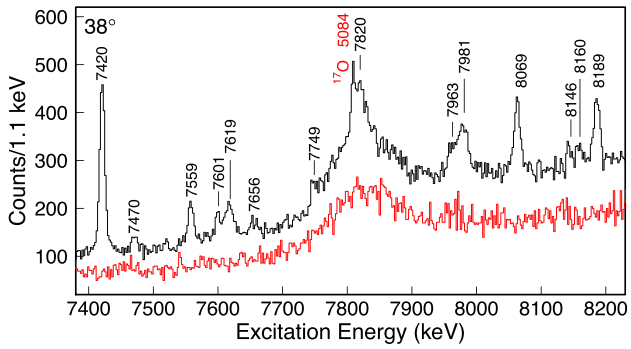

Figure 1. A proton focal-plane position spectrum from the ^{20}Ne(d, p)^{21}Ne reaction at $\theta_{lab} = 38°$. Peaks are labelled with their corresponding excitation energy in ^{21}Ne (keV). The carbon spectrum (arbitrary scale) is shown in red, highlighting the location of the ^{17}O background contamination peak.

collecting ^{20}Ne(d, p)^{21}Ne data at each angle to account for any target degradation. Uncertainties in neon target areal density were of the order of 7 per cent.

Reaction products entered the TUNL Enge split-pole spectrograph through a 0.54 ± 0.01 msr aperture and were momentum analyzed at the focal plane. The focal-plane detector comprised of two position-sensitive gas avalanche counters, a ΔE proportional counter, and a scintillation counter (Marshall et al. 2018). Protons were identified using a ΔE-position cut. Data were collected at five laboratory angles: 10°, 15°, 20°, 25°, and 38°. Additional data for background characterization were collected using a natural carbon target at each angle.

A quadratic internal calibration using the ^{21}Ne states at E_x = 6609(1), 7420(1), 8069(2), and 8189(2) keV (Firestone 2015) was used to convert focal-plane position to excitation energy. The Bayesian method outlined by Marshall et al. (2018) gave realistic E_x uncertainties, explicitly including the statistical uncertainties in the fitted peak centroids and the systematic uncertainties from the focal-plane calibration. For peaks observed at multiple angles, our recommended energy was obtained from a weighted average of individual measurements. The reported energy uncertainty was conservatively constrained to be no smaller than the uncertainty at a single angle.

An example focal-plane spectrum for the astrophysically important region is shown in Fig. 1. To extract peak intensities and positions, the focal plane was divided into regions based on the behaviour of the background reactions determined from the carbon target. For more details on the peak fitting, see Frost-Schenk (2020). Angular distributions were extracted from the yields for each state observed at each angle accounting for beam on target, aperture solid angle, target content and dead time, which was typically below 9 per cent.

4 CALCULATION OF NEUTRON WIDTHS

The code FRESCO (Thompson 1988) was used to calculate differential cross-sections under the assumption of a single-step reaction, in order to assign the transferred angular momentum, ℓ_n, and extract the neutron width, Γ_n. Calculations were performed using the first-order distorted-wave Born approximation since at these low energies the breakup effects on the deuteron in the entrance channel are minimal (Johnson & Soper 1970). Past ^{20}Ne(d, p)^{21}Ne transfer reactions reported in Stanford & Quin (1980) have observed significant

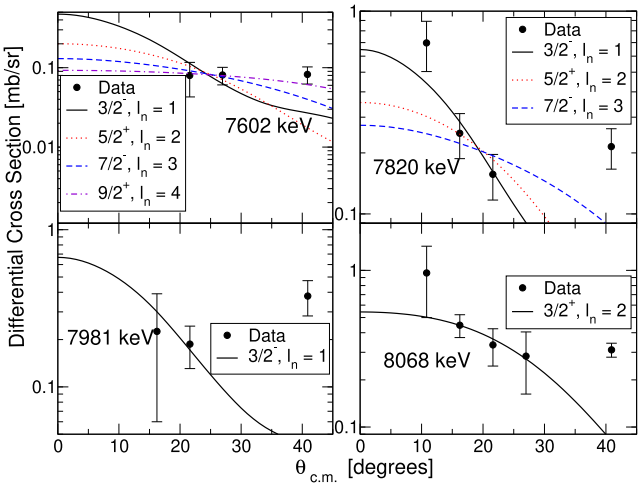

Figure 2. Experimental differential cross-sections for some of the relevant states discussed in the present work. The 7981- and 8068-keV states have known J^π (Cohn & Fowler 1959; Firestone 2015) while the 7602- and 7820-keV states have unknown J^π. Note that, while the 38° data are included in the plot, they are not used in the DWBA analysis.

deviation between the expected differential cross-section and the observed data at angles higher than $\theta_{\rm lab} = 25°$. For this reason, $\theta_{\rm lab} = 38°$ data was not used to assign ℓ_n. The $\theta_{\rm lab} = 38°$ data were used to determine E_x and constrain the total width for observed states.

The optical model potentials for ^{20}Ne+d, ^{21}Ne+p, ^{20}Ne+n, n + p, and ^{20}Ne+p were taken from An & Cai (2006), Varner et al. (1991), Madland (1997), Yahiro et al. (1986) and Menet et al. (1971), respectively. Spectroscopic factors (C^2S) relating the DWBA and experimental cross-sections

$$\frac{{\rm d}\sigma}{{\rm d}\Omega}_{\rm exp} = C^2S\frac{{\rm d}\sigma}{{\rm d}\Omega}_{\rm DWBA} \quad (1)$$

were found by normalizing the calculations to the experimental data. Example differential cross-sections for four states are shown in Fig. 2. Two states with known J^π (the $J^\pi = \frac{3}{2}^-$, $E_x = 7981$-keV state and $J^\pi = \frac{3}{2}^+$, 8068-keV state) have been included to demonstrate that the DWBA calculations reproduce the data well. Two states with inconclusive J^π assignments are also shown.

The wave-functions from FRESCO, $\phi(r)$, were used to compute the neutron widths, Γ_n as in Iliadis (1997),

$$\Gamma_n = 2P_\ell(E_n, a)\frac{\hbar^2 a}{2\mu}C^2S\,|\phi(a)|^2, \quad (2)$$

where $P_\ell(E_n, a)$ is the penetrability of a neutron of energy E_n and orbital angular momentum ℓ evaluated at the radius a; μ is the reduced mass. The radius, a, was chosen to be where the ^{20}Ne+n wave-function is at 99 per cent of the asymptotic value (Meyer et al. 2020) and varied for different binding energies and ℓ_n. We used the weak-binding approximation, calculating at various positive binding energies and extrapolating with a quadratic function to the negative, physical neutron binding energy (Meyer et al. 2020). The uncertainties resulting from the calculations are much smaller than the uncertainty in the absolute normalization from other sources.

5 EVALUATION OF ^{17}O+α REACTION RATES

Table 1 summarizes the spectroscopic information on relevant states in ^{21}Ne above the α-particle threshold. We discuss below the spin-parity assignments of astrophysically important states from which

Downloaded from https://academic.oup.com/mnras/article/514/2/2650/6589423 by guest on 01 July 2022

Table 1. Spectroscopic information for relevant states above the α-particle threshold in ^{21}Ne. Previous excitation energies from other sources are given in the second column. The neutron partial widths (Γ_n) are those determined in the present experiment. Widths given in bold are measured or experimentally constrained values. The $\Gamma_\gamma = 0.20(14)$ eV are taken from the average of measured lifetimes in Rolfs et al. (1972) except where noted in the final column to preserve the Γ_n/Γ_γ ratio of Best et al. (2013) for resonances for which no updated information is available. Resonance information on higher resonances is taken from Best et al. (2013).

E_x [keV]	Previous E_x [keV]	$E_{r,\alpha}$ [keV]	$2J^\pi$	ℓ_α	ℓ_n	Γ_α [eV]	Γ_n [eV]	Comments
7420.4(15)*	7420.3(10)	72.5(15)	$(5, 7)^-$	1	3	1.2×10^{-33}	**14(1)**, **11(1)**	
7470(2)	7465(10)	122(2)	$(1, 3)^-$	3,1	1	7.9×10^{-24}, 3.9×10^{-22}	200(140)	Adopt $\frac{\Gamma_\gamma}{\Gamma_n} = 10^{-3}$[a]
7559.1(15)	7547(10)	211.2(15)	$(3, 5)^+$	2,0	2,2	2.4×10^{-14}, 2.5×10^{-13}	**570(30)**, **420(20)**	
7602.0(15)	7600(5)	254.1(15)	$(5, 7)^-$	1	3	2.6×10^{-11}	**8(2)**, **6(2)**	
			$(7, 9)^+$	2	4	5.6×10^{-12}	**0.4(1)**, **0.3(1)**	
7619.9(10)	7628(10)	272.0(10)	3^{-f}	1	1	1.7×10^{-10}	**8000(1000)**	
7655.7(22)	7648(2)	307.8(22)	7^{+h}	2	4	9.8×10^{-10}	0.10(7)	Adopt $\frac{\Gamma_\gamma}{\Gamma_n} = 2$[a]
7748.8(17)	7740(10)	400.9(17)	5^{+a}	0	2	5.2×10^{-6}	200(140)	Adopt $\frac{\Gamma_\gamma}{\Gamma_n} = 10^{-3}$[a]
7820.1(15)	7810(10)	472.2(15)	$(3, 5)^+$	2,0	2	1.8×10^{-5}, 1.7×10^{-4}	**560(90)**, **400(60)**	
7960(2)	7960.9(13)	612(2)	11^{-g}	3	5	5.3×10^{-8}	0.10(7)	Adopt $\frac{\Gamma_\gamma}{\Gamma_n} = 2$[a]
7981(2)	7980(10)	633(2)	3^{-f}	1	1	1.9×10^{-2}	**14000(5000)**	
7982.1(7)	7982.1(6)	634.2(7)				$7.5(15) \times 10^{-6}$		From $\omega\gamma_{(\alpha,\gamma)} = 4.98(97)$ μeV[e]
8008(2)	8009(10)	660(2)	1^{-f}	3	1	1.2×10^{-3}	0.20(14)	$\Gamma_\gamma = 2.0(14) \times 10^{-4}$ eV
8069(1)*	8069(2)	721(1)	3^{+a}	2	2	**46.2(46)** $\times$ **10^{-3}**	**1600(200)**	$\Gamma_\gamma = 0.54(35)$ eV[d]
8146(1)	8146(2)	798(1)	3^{+a}	2,0	2	**54.7(55)** $\times$ **10^{-3}**	**550(150)**, **400(100)**	
8159(2)[b]	8155.0(10)	811(2)	9^{+g}	2	4			$\omega\gamma_{(\alpha,,\gamma)} = 7.72(55)$[c] meV
8160(2)	8160(2)	812(2)	5^{+a}	0	2	**1.6(2)** $\times$ **10^{-3}**	**23000(2300)**	Adopted from Ref.?

*: used in calibration
a: Best et al. (2013)
b: Best et al. (2011)
c: Weighted average of Williams et al. (2022) and Best et al. (2011).
d: To preserve the measured $\omega\gamma_{(\alpha,\gamma)}$ from Ref. Williams et al. (2022).
e: Williams et al. (2022)
f: Cohn & Fowler (1959)
g: Thummerer et al. (2003)
h: Hoffman et al. (1989)

we produce physically motivated reaction rates, with uncertainties for the first time. A comprehensive discussion on all of the states observed in this work will be presented in a forthcoming paper.

The E_x = 7559-, 7820-, 8146-, and 8189-keV states all have differential cross-sections which are consistent with $\ell_n = 1$ or 2 assignments. For $\ell_n = 1$ the Γ_n are, for $J^\pi = \frac{1}{2}^-$, 25(1), 20(3), 19(5), and 130(13), respectively (for $J^\pi = \frac{3}{2}^-$, Γ_n = 14(1), 11(2), 11(3), and 74(7) keV, respectively). Resonances with Γ_n of this size would both have been observed in the neutron-scattering study reported in Cohn & Fowler (1959) and would additionally result in visible broadening of the states in the focal-plane spectrum. Since neither of these are observed, $\ell_n = 1$ is ruled out for all of these states.

The differential cross-section of the E_x = 7602-keV state is consistent with ℓ_n = 2–4. This state has been observed in γ-ray data of Rolfs et al. (1972). An $\ell_n = 2$ assignment results in a neutron width of more than 100 eV. Based on lifetimes reported in that work, this neutron width greatly exceeds realistic γ-ray partial widths. It is therefore unlikely that γ-ray decay from this state would be observed if the $\ell_n = 2$ assignment were made. We therefore assign this level $\ell_n = 3$ or $\ell_n = 4$.

Close to E_x = 7982 keV are two states, one narrow at E_x = 7982.1(6) keV (Firestone 2015; Taggart et al. 2019), likely not observed in this experiment, and a broader one at $E_x = 7981(2)$ keV, likely the state populated in the present work. The neutron width (Γ_n = 6(2) keV), spin, and parity ($J^\pi = \frac{3}{2}^-$) of the E_x = 7981(2)-keV state are known from ^{20}Ne+n resonance scattering (Cohn & Fowler 1959). From the current data, we determine Γ_n = 14(5) keV.

Reaction rates were calculated using the RATESMC Monte Carlo code (Longland et al. 2010; Sallaska et al. 2013). Data on directly measured ^{17}O(α, γ)^{21}Ne and ^{17}O(α, n)^{20}Ne resonances were taken from Best et al. (2011,2013) and Williams et al. (2022). The weighted mean with inflated uncertainties described by Longland, Iliadis & Karakas (2012) was used for the ^{17}O(α, γ)^{21}Ne resonance strengths to account for systematic uncertainties. For many of the resonances listed in Best et al. (2013) there are no listed uncertainties. These were arbitrarily assumed to be 10 per cent for all widths. For any resonances for which all partial widths could be estimated, the reaction rate was numerically integrated.

For resonances with no measured Γ_α, the reduced α-particle width was sampled from a Porter-Thomas distribution (see Longland et al. 2012; Sallaska et al. 2013 for details). The neutron widths were, where available, taken from the present work. Γ_γ = 0.20(14) eV was used, from the average of the lifetimes in Rolfs et al. (1972). For resonances where the Γ_n and Γ_γ are unknown, the ratio of these widths is adopted from Best et al. (2013). Importantly, we adopt the tentative $J^\pi = \frac{7}{2}^+$ assignment for the E_r = 308-keV resonance from Firestone (2015) which reduces the contribution of this state to the ^{17}O(α, γ)^{21}Ne reaction rate compared to Best et al. (2013) in which a $J^\pi = \frac{5}{2}^+$ assignment was used. We furthermore note that a $\frac{5}{2}^+$ assignment is inconsistent with systematic trends in ^{21}Ne in

Downloaded from https://academic.oup.com/mnras/article/514/2/2650/6589423 by guest on 01 July 2022

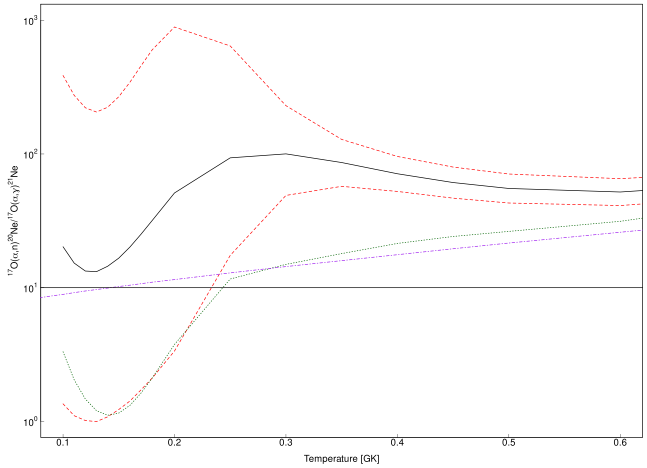

Figure 3. The ratios of the $^{17}O(\alpha, n)^{20}Ne$ and $^{17}O(\alpha, \gamma)^{21}Ne$ reaction rates. The solid black line shows the ratio of the median rates in the current calculation and the dashed red lines show the ratios of the upper (lower) $^{17}O(\alpha, n)^{20}Ne$ rate to the lower (upper) $^{17}O(\alpha, \gamma)^{21}Ne$ reaction rates. The green dotted line shows the ratio of the rates from Best et al. (2013) The purple dash–dotted line shows the ratio of the rates from Caughlan & Fowler (1988).

which no other $J^{\pi} = \frac{5}{2}^{+}$ states at a similar excitation energy decay by γ-ray emission.

The $E_x = 7749$-keV state was only observed at one angle due to ^{16}O contamination. The peak observed in the present experiment does not appear in the background spectrum and was therefore assumed to be a ^{21}Ne state, but confirmation of this state with additional measurements is required. An angular distribution could not be extracted and the spin remains unconstrained. For the calculation of the rate we adopted the assumptions of Best et al. (2013).

For the $^{17}O(\alpha, \gamma)^{21}Ne$ reaction, the Monte Carlo calculations show that the dominant contributions are from the resonances at $E_r = 308$, 634, and 811 keV ($E_x = 7656$, 7961, 7982, and 8159 keV). The 634- and 811-keV resonances have measured strengths (Best et al. 2011; Taggart et al. 2019; Williams et al. 2022). For the $^{17}O(\alpha, n)^{20}Ne$ reaction, the dominant contributions are from the $E_r = 401$-, 472-, and 721-keV resonances ($E_x = 7749$, 7820, and 8069 keV) with a small contribution from the $E_r = 633$-keV resonance. The dominant contributions to the uncertainty in the reaction-rate ratio are the unknown Γ_α partial widths.

The $^{17}O(\alpha, n)^{20}Ne$ to $^{17}O(\alpha, \gamma)^{21}Ne$ reaction-rate ratio for our median rates is presented in Fig. 3. Also shown are 1σ 'high' and 'low' ratios from our work, and those from Caughlan & Fowler (1988) and Best et al. (2013). The present ratio is significantly higher than that of Best et al. between 0.25 and 0.7 GK for a number of reasons. There are some inconsistencies in the data in Table II of Best et al. (2013; e.g. the $E_r = 308$-keV resonance state) for which the listed resonance strengths are in disagreement with the Γ_n and Γ_γ ratio (Best, Private Communication). We have, additionally, changed spin-parity assignments where appropriate resulting in some changes in contributions of states to the reaction rates. Lastly, we have utilized the direct $^{17}O(\alpha, \gamma)^{21}Ne$ measurements from DRAGON (Williams et al. 2022).

Contribution plots for the two reactions are shown in Fig. 4 (see caption for details). For the $^{17}O(\alpha, \gamma)^{21}Ne$ reaction, the main contribution within the astrophysically relevant region is the $E_r = 308$-keV resonance, for which no estimate of the α-particle width is yet available. More resonances can potentially contribute to the

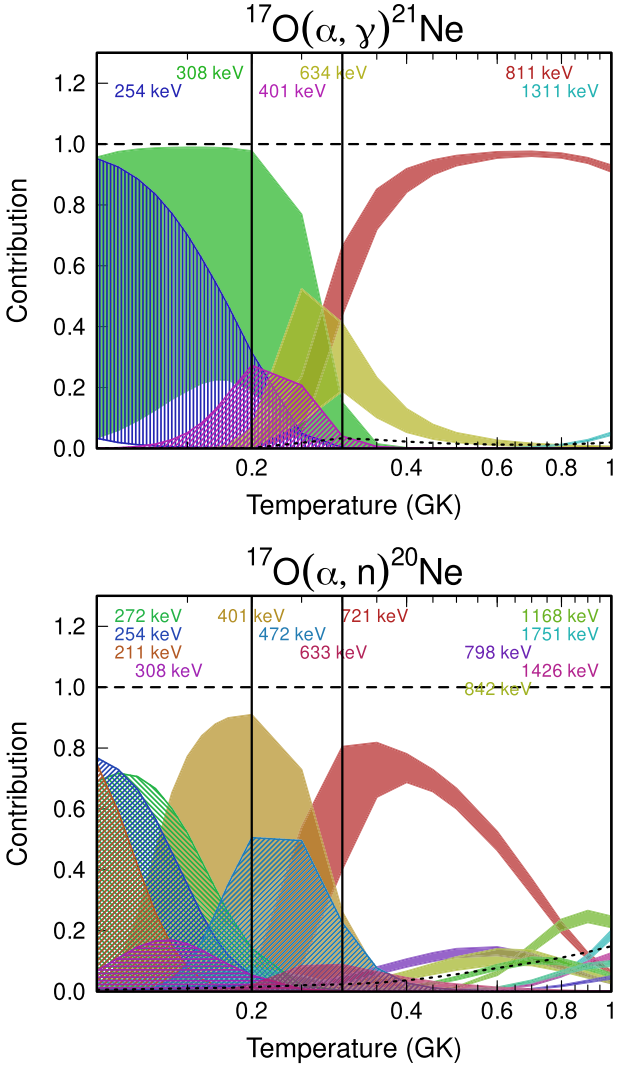

Figure 4. Contribution plots for (top) the $^{17}O(\alpha, \gamma)^{21}Ne$ reaction and (bottom) the $^{17}O(\alpha, n)^{20}Ne$ reaction indicating which resonances dominate the reaction rate within the Gamow window (vertical lines). The coloured bands show the uncertainty in the contribution of each resonance to the total rate.

$^{17}O(\alpha, n)^{20}Ne$ reaction, since for many of these resonances the neutron partial width is known to be much larger than the γ-ray partial width. For most resonances therefore the γ-ray decay is vanishingly small and these states cannot meaningfully contribute to the flux of abundances through the $^{17}O(\alpha, \gamma)^{21}Ne$ reaction.

The $^{17}O(\alpha, \gamma)^{21}Ne$ and $^{17}O(\alpha, n)^{20}Ne$ reaction rates are shown in Tables 2 and 3, respectively.

6 ASTROPHYSICAL IMPLICATIONS

We tested the impact of the new $^{17}O(\alpha, n)^{20}Ne$ and $^{17}O(\alpha, \gamma)^{21}Ne$ rates on s-process nucleosynthesis using a simplified one-zone nucleosynthesis code mimicking core helium burning. Details on this code can be found in Choplin et al. (2016). The code was also used in Placco et al. (2020) to make comparisons with an observed star enriched in trans-iron elements. We follow the central temperature and density profiles obtained from a complete rotating 25 $M_\odot$ stellar model at a metallicity of 10^{-3} in mass fraction, computed with the

Downloaded from https://academic.oup.com/mnras/article/514/2/2650/6589423 by guest on 01 July 2022

Table 2. The $^{17}O(\alpha, \gamma)^{21}Ne$ reaction rate. The lower, median, and upper columns correspond to the 32 per cent, 50 per cent, and 68 per cent intervals for the computed reaction rate. The reaction rates are in units of cm^3 mol^{-1} s^{-1}.

T [GK]	Lower	Recommended	Upper
0.100	2.18×10^{-22}	1.20×10^{-21}	5.33×10^{-21}
0.110	3.67×10^{-21}	2.05×10^{-20}	9.19×10^{-20}
0.120	3.91×10^{-20}	2.21×10^{-19}	1.01×10^{-18}
0.130	2.94×10^{-19}	1.68×10^{-18}	7.95×10^{-18}
0.140	1.68×10^{-18}	9.59×10^{-18}	4.66×10^{-17}
0.150	7.71×10^{-18}	4.38×10^{-17}	2.18×10^{-16}
0.160	3.00×10^{-17}	1.67×10^{-16}	8.43×10^{-16}
0.170	1.01×10^{-16}	5.46×10^{-16}	2.81×10^{-15}
0.180	2.99×10^{-16}	1.59×10^{-15}	8.22×10^{-15}
0.200	2.13×10^{-15}	1.02×10^{-14}	5.13×10^{-14}
0.250	3.23×10^{-13}	5.84×10^{-13}	1.71×10^{-12}
0.300	4.54×10^{-11}	5.53×10^{-11}	6.94×10^{-11}
0.350	2.43×10^{-09}	2.70×10^{-09}	3.02×10^{-09}
0.400	5.24×10^{-08}	5.68×10^{-08}	6.18×10^{-08}
0.450	5.76×10^{-07}	6.21×10^{-07}	6.69×10^{-07}
0.500	3.90×10^{-06}	4.19×10^{-06}	4.50×10^{-06}
0.600	6.74×10^{-05}	7.21×10^{-05}	7.71×10^{-05}
0.700	5.03×10^{-04}	5.37×10^{-04}	5.72×10^{-04}
0.800	2.23×10^{-03}	2.37×10^{-03}	2.53×10^{-03}
0.900	7.04×10^{-03}	7.48×10^{-03}	7.95×10^{-03}
1.000	1.76×10^{-02}	1.87×10^{-02}	1.98×10^{-02}

Table 3. As Table 2 but for the $^{17}O(\alpha, n)^{20}Ne$ reaction.

T [GK]	Lower	Recommended	Upper
0.100	7.04×10^{-21}	2.52×10^{-20}	8.75×10^{-20}
0.110	9.98×10^{-20}	3.24×10^{-19}	1.05×10^{-18}
0.120	1.01×10^{-18}	3.00×10^{-18}	9.13×10^{-18}
0.130	7.92×10^{-18}	2.22×10^{-17}	6.40×10^{-17}
0.140	5.02×10^{-17}	1.38×10^{-16}	3.91×10^{-16}
0.150	2.66×10^{-16}	7.30×10^{-16}	2.14×10^{-15}
0.160	1.20×10^{-15}	3.40×10^{-15}	1.07×10^{-14}
0.170	4.75×10^{-15}	1.42×10^{-14}	4.78×10^{-14}
0.180	1.70×10^{-14}	5.30×10^{-14}	1.91×10^{-13}
0.200	1.70×10^{-13}	5.58×10^{-13}	2.23×10^{-12}
0.250	3.63×10^{-11}	7.30×10^{-11}	2.35×10^{-10}
0.300	4.72×10^{-09}	5.78×10^{-09}	9.44×10^{-09}
0.350	1.92×10^{-07}	2.15×10^{-07}	2.57×10^{-07}
0.400	3.24×10^{-06}	3.54×10^{-06}	3.95×10^{-06}
0.450	2.99×10^{-05}	3.23×10^{-05}	3.54×10^{-05}
0.500	1.80×10^{-04}	1.94×10^{-04}	2.10×10^{-04}
0.600	2.90×10^{-03}	3.08×10^{-03}	3.28×10^{-03}
0.700	2.46×10^{-02}	2.59×10^{-02}	2.72×10^{-02}
0.800	1.49×10^{-01}	1.55×10^{-01}	1.61×10^{-01}
0.900	7.29×10^{-01}	7.56×10^{-01}	7.84×10^{-01}
1.000	$3.03 \times 10^{+00}$	$3.13 \times 10^{+00}$	$3.25 \times 10^{+00}$

Geneva stellar evolution code (Eggenberger et al. 2008). The initial composition of the one-zone code is extracted from the core of this stellar model, at core helium-burning ignition. To mimic rotation, ^{13}C and ^{14}N are injected (cf. Section 1) at a constant rate (expressed in M$_\odot$ yr^{-1}) during the nucleosynthesis calculation (Choplin et al. 2016). During injection, 100 times more ^{14}N as ^{13}C is injected as a typical value in full stellar models (e.g. fig. 9 in Choplin et al. 2018). This factor of ∼100 corresponds to the CNO ^{14}N/^{13}C equilibrium ratio at $T \sim 80$ MK, which is found at the bottom of the H-burning shell in massive stars. The injection rate was calibrated so as to reproduce the central abundances of a full rotating stellar model at the end of the core helium-burning phase. For this calibration, we used the same rates as in the full stellar model, namely the rates of Best et al. (2013) for $^{17}O(\alpha, \gamma)^{21}Ne$ and $^{17}O(\alpha, n)^{20}Ne$, the rates of Longland et al. (2012) for $^{22}Ne(\alpha, \gamma)^{26}Mg$ and $^{22}Ne(\alpha, n)^{25}Mg$, and the rate from Guo et al. (2012) for $^{13}C(\alpha, n)^{16}O$. The adopted standard injection rate is 2.5×10^{-7} M$_\odot$ yr^{-1} and produces the overproduction factors[1] shown by the solid red line in Fig 5. For most elements, it deviates by less than 5 per cent from the full model (green pattern). Cases with higher (red dotted line) and lower (red dashed line) injection rates are shown for comparison. Without injection, we obtain a typical weak s-process pattern from non-rotating massive stars (black pattern).

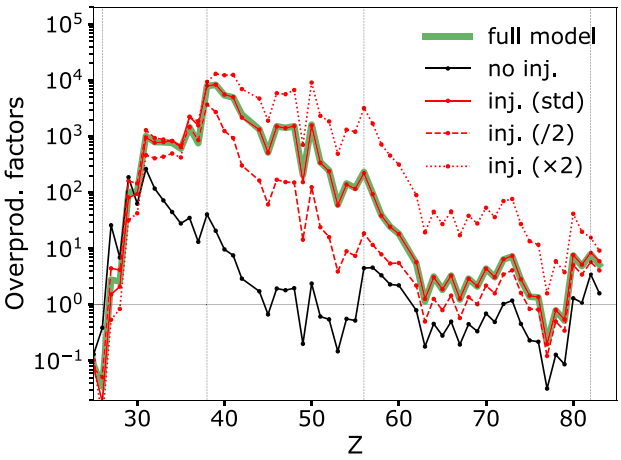

Figure 5. Overproduction factors of a one zone nucleosynthesis model mimicking the core helium burning phase of a rotating massive star at low metallicity. Different injection cases (see text for details) are considered: no injection (black pattern) and injection at three different rates (red patterns). The green pattern shows the outputs of the central layer of a full stellar model at the end of the core helium-burning stage. Here all models were computed with the rates of Best et al. (2013) for $^{17}O(\alpha, \gamma)$ and $^{17}O(\alpha, n)$. The four vertical lines highlight the elements Fe, Sr, Ba, and Pb.

In the left-hand panel of Fig. 6, all one-zone models were computed with the standard injection rate of 2.5×10^{-7} M$_\odot$ yr^{-1} obtained from the calibration discussed previously. The only differences between the models shown in Fig. 6 (left-hand panel) and the model shown by the solid red line in Fig. 5 are the rates of $^{17}O(\alpha, n)^{20}Ne$ and $^{17}O(\alpha, \gamma)^{21}Ne$. The recommended reaction rates were used (fs21), as well as the limiting cases of the minimum (fs21_min) and maximum (fs21_max) $(\alpha, n)/(\alpha, \gamma)$ ratio. These results show that the s-process in rotating massive stars is likely to continue at least to barium, and potentially up to lead for the largest $(\alpha, n)/(\alpha, \gamma)$ reaction-rate ratio. The scatter for elements with atomic number $Z > 40$ goes up to about 2 dex. The bg13 and fs21_min sets have the lowest $^{17}O(\alpha, n)^{20}Ne/^{17}O(\alpha, \gamma)^{21}Ne$ ratios (Fig. 3) hence giving the lowest yields (green and red dotted pattern). The cf88 and fs21 sets with higher $(\alpha, n)/(\alpha, \gamma)$ ratios substantially produce elements with $Z > 55$ and the fs21_max set shows the highest yields, as expected from the high $(\alpha, n)/(\alpha, \gamma)$ ratio.

As an estimate of the impact of the new rate at very low metallicity, we include in the right-hand panel of Fig. 6 a one-zone calculation similar to the fs21 model (black pattern) but computed with an initial

[1]The overproduction factors are expressed as X_f/X_i where $X_{i/f}$ represent the initial/final mass fractions.

Downloaded from https://academic.oup.com/mnras/article/514/2/2650/6589423 by guest on 01 July 2022

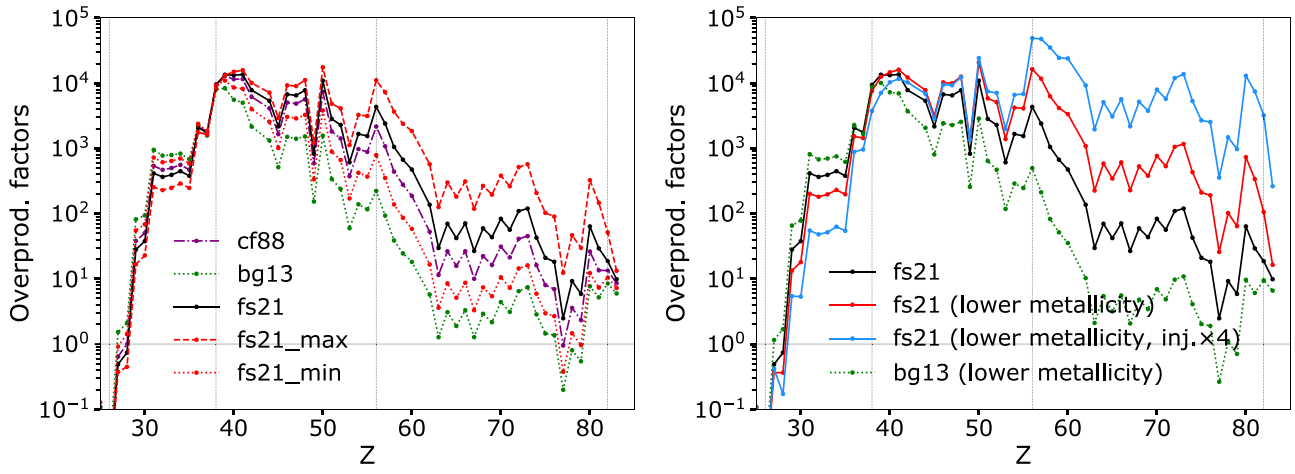

Figure 6. Overproduction factors of a one zone nucleosynthesis model mimicking the core helium burning phase of a rotating massive star **at low metallicity.** Left-hand panel: The five sets of rates shown in Fig. 3 are tested: cf88 (Caughlan & Fowler 1988), bg13 (Best et al. 2013), the recommended rates derived in this work (fs21) plus the two limiting cases shown in Fig. 3. The four vertical lines highlight the elements Fe, Sr, Ba, and Pb. Right-hand panel: The fs21 model at a metallicity of 10^{-3} in mass fraction is shown again (black pattern) together with the same model but with initial abundances corresponding to a metallicity of 10^{-5} (red pattern). The blue model is computed like the red one but with an injection rate four times higher. The bg13 model at a metallicity of 10^{-5} is also shown.

composition corresponding to a metallicity of 10^{-5} in mass fraction (red pattern). This shows that a lower initial metallicity combined with a similar neutron production leads to a stronger overproduction of elements heavier than atomic number $Z \sim 50$ at the expense of lighter elements. This is even more visible if considering a higher injection rate (green pattern) which would correspond to a more efficient rotational mixing in full stellar models. A higher injection rate at lower metallicity is not unrealistic since rotational mixing is expected to be more efficient with decreasing metallicity (e.g. Maeder & Meynet 2001). We note that contrary to the fs21 rates, the bg13 rates at lower metallicity do not lead to significant changes in the overproduction factors (compare the green patterns in the two panels of Fig. 6). Full stellar models would be required to get a more accurate estimate of the overproduction factors.

7 CONCLUSIONS

For the first time, available data on the energies, spins, parities, and partial widths of excited states in ^{21}Ne have been thoroughly evaluated including a careful consideration of their ambiguities and uncertainties. In addition, states in ^{21}Ne have been populated via the ^{20}Ne$(d, p)^{21}$Ne reaction, using an implanted ^{20}Ne target. Angular distributions and neutron widths for states within the Gamow window for massive-star He-core burning were extracted. By combining these data with the evaluated data, reaction rates for ^{17}O$(\alpha, n)^{20}$Ne and ^{17}O$(\alpha, \gamma)^{21}$Ne have been calculated using updated excitation energies, J^{π} assignments, and experimentally derived neutron widths. Using the RATESMC Monte Carlo code, uncertainties have been estimated consistently for the first time. Our recommended rates indicate enhanced s-process abundances between Sr and Pb. Production of these elements via the enhanced weak s-process in massive stars significantly shortens the time-scale for the production of Pb (otherwise only produced via the main s-process in low-mass stars with much longer lifetimes) and provides an alternative to the r-process for producing elements between Fe and Ba in the early Universe. Experimental constraints on the α-widths of the key states in ^{21}Ne are thus crucial to allow the production of elements above barium in such massive stars, and so for the evolution of elements heavier than iron in the early Universe to be understood.

ACKNOWLEDGEMENTS

The authors thank Nick Keeley and Andreas Best for useful discussions. JFS, AML, CB, and CD thank the UK Science and Technology Facilities Council (STFC). PA thanks the trustees and staff of Claude Leon Foundation for support in the form of a Postdoctoral Fellowship. RL, CM, FP, and KS thank the U.S. Department of Energy, Office of Science, Office of Nuclear Physics, for support under Grant No. DE-SC0017799 and Contract Nos. DE-FG02-97ER41033 and DE-FG02-97ER41042. This work was supported by the Fonds de la Recherche Scientifique-FNRS under Grant No. IISN 4.4502.19. This paper is based upon work from the 'ChETEC' COST Action (CA16117), supported by COST (European Cooperation in Science and Technology). RH acknowledges support from the IReNA AccelNet Network of Networks, supported by the National Science Foundation under Grant No. OISE-1927130 and from the World Premier International Research Centre Initiative (WPI Initiative), MEXT, Japan. RH also acknowledges funding from the European Union's Horizon 2020 research and innovation programme under grant agreement No 101008324 (ChETEC-INFRA).

DATA AVAILABILITY

The nuclear physics data used in the evaluation are available from NNDC (https://www.nndc.bnl.gov) via ENSDEF and EXFOR. The reaction rates in tabular form will be available as part of the Starlib reaction rate library (https://github.com/Starlib/Rate-Library). Other data arising from the present work are available on reasonable request to the corresponding author.

REFERENCES

An H., Cai C., 2006, Phys. Rev. C, 73, 054605
Andritsopoulos G., Catford W., Garman E., Pringle D., Fifield L., 1981, Nucl. Phys. A, 372, 281

Downloaded from https://academic.oup.com/mnras/article/514/2/2650/6589423 by guest on 01 July 2022

Banerjee P., Heger A., Qian Y.-Z., 2019, ApJ, 887, 187
Baraffe I., El Eid M. F., Prantzos N., 1992, A&A, 258, 357
Best A., 2021, Private Communication
Best A. et al., 2011, Phys. Rev. C, 83, 052802
Best A. et al., 2013, Phys. Rev. C, 87, 045805
Caughlan G. R., Fowler W. A., 1988, At. Data Nucl. Data Tables, 40, 283
Cescutti G., Chiappini C., Hirschi R., Meynet G., Frischknecht U., 2013, A&A, 553, A51
Choplin A., Maeder A., Meynet G., Chiappini C., 2016, A&A, 593, A36
Choplin A., Hirschi R., Meynet G., Ekström S., Chiappini C., Laird A., 2018, A&A, 618, A133
Cohn H. O., Fowler J. L., 1959, Phys. Rev., 114, 194
Dudek A., Edens D., 1971, Phys. Lett. B, 36, 309
Eggenberger P., Meynet G., Maeder A., Hirschi R., Charbonnel C., Talon S., Ekström S., 2008, Ap&SS, 316, 43
Firestone R. B., 2015, Nucl. Data Sheets, 127, 1
Frischknecht U., Hirschi R., Thielemann F.-K., 2012, A&A, 538, L2
Frischknecht U. et al., 2016, MNRAS, 456, 1803
Frost-Schenk J. W., 2020, PhD thesis, University of York, available at http://etheses.whiterose.ac.uk/28004/
Guo B. et al., 2012, ApJ, 756, 193
Hallock J., Enge H., Garrett J., Middleton R., Fortune H., 1975, Nucl. Phys. A, 252, 141
Hoffman A. et al., 1989, Z. Phys. A., 332, 289
Iliadis C., 1997, Nucl. Phys, A, 618, 166
Johnson R. C., Soper P. J. R., 1970, Phys. Rev. C, 1, 976
Langer N., Arcoragi J.-P., Arnould M., 1989, A&A, 210, 187
Limongi M., Chieffi A., 2018, ApJS, 237, 13
Longland R., Iliadis C., Champagne A. E., Newton J. R., Ugalde C., Coc A., Fitzgerald R., 2010, Nucl. Phys. A, 841, 1
Longland R., Iliadis C., Karakas A. I., 2012, Phys. Rev. C, 85, 065809
Madland D. G., 1997, OECD/NEA report# LA-UR-97-0306
Maeder A., Meynet G., 2001, A&A, 373, 555
Marshall C., Setoodehnia K., Kowal K., Portillo F., Champagne A. E., Hale S., Dummer A., Longland R., 2018, IEEE Trans. Instrum. Meas., 68, 533
Menet J., Gross E., Malanify J., Zucker A., 1971, Phys, Rev. C, 4, 1114
Meyer A. et al., 2020, Phys. Rev. C, 102, 035803
Mohr P., 2017, Phys. Rev. C, 96, 045808
Pignatari M., Gallino R., Meynet G., Hirschi R., Herwig F., Wiescher M., 2008, ApJ, 687, L95
Placco V. M. et al., 2020, ApJ, 897, 78
Prantzos N., Hashimoto M., Nomoto K., 1990, A&A, 234, 211
Raiteri C. M., Busso M., Picchio G., Gallino R., 1991, ApJ, 371, 665
Rolfs C., Trautvetter H., Kuhlmann E., Riess F., 1972, Nucl. Phys. A, 189, 641
Sallaska A. L., Iliadis C., Champange A. E., Goriely S., Starrfield S., Timmes F. X., 2013, ApJS, 207, 18
Stanford A., Quin P., 1980, Nucl. Phys. A, 342, 283
Taggart M. et al., 2019, Phys. Lett. B, 798, 134894
The L.-S., El Eid M. F., Meyer B. S., 2007, ApJ, 655, 1058
Thielemann F. K. et al., 2011, Prog. Part. Nucl. Phys., 66, 346
Thompson I. J., 1988, Comput. Phys. Rep., 7, 167
Thummerer S. et al., 2003, J. Phys. G: Nucl. Part. Phys., 29, 509
Varner R., Thompson W., McAbee T., Ludwig E., Clegg T., 1991, Phys. Rep., 201, 57
Wheldon C. et al., 2005, Eur. Phys. J. A, 26, 321
Williams M. et al., 2022, Phys. Rev. C, preprint (arXiv:2206.06016)
Yahiro M., Iseri Y., Kameyama H., Kamimura M., Kawai M., 1986, Prog. Theor. Phys. Suppl., 89, 32

This paper has been typeset from a TEX/LATEX file prepared by the author.

Downloaded from https://academic.oup.com/mnras/article/514/2/2650/6589423 by guest on 01 July 2022